Korean J. Chem. Eng., 39(7), 1788-1795 (2022)
DOI: 10.1007/s11814-022-1123-2

pISSN: 0256-1115
eISSN: 1975-7220

One-step synthesis of Ni_3N@C hybrid and its catalytic activity for overall water splitting

Weilin Weng*,,***, Jianhong Chen*,**,***, Qingcui Liu*,**,***, Feng Yu*, Jianning Wu*,**, Zhiyong Liu*,**, and Banghua Peng*,**,***,†**

*School of Chemistry and Chemical Engineering/Key Laboratory for Green Processing of Chemical Engineering of Xinjiang Bingtuan, Shihezi University, Shihezi, 832003, P. R. China
**Key Laboratory of Materials-Oriented Chemical Engineering of Xinjiang Uygur Autonomous Region/Engineering Research Center of Materials-Oriented Chemical Engineering of Xinjiang Bingtuan, Shihezi University, Shihezi, 832003, P. R. China
***Clean Energy Conversion and Storage Research Group, Shihezi University, Shihezi, 832003, P. R. China
(*Received 8 December 2021 • Revised 12 March 2022 • Accepted 23 March 2022*)

Abstract−Ni_3N@C nanocomposite was prepared by a simple one-step low-temperature pyrolysis method with nickel acetate in flowing ammonia. The spherical Ni_3N nanoparticles were uniformly coated with a carbon protective layer formed in-situ with a thickness of 10 nm, which shows excellent catalytic activity for overall water splitting in alkaline solution. The experimental results showed that the initial potential for hydrogen evolution reaction (HER) was −0.06 V (versus reversible hydrogen electrode, vs RHE), and the overpotential (η) was 284 mV at the current density of 10 mA cm^{-2}; the initial potential for oxygen evolution reaction (OER) was 1.53 V vs RHE, and η was 390 mV at the current density of 10 mA cm^{-2}. In addition, Ni_3N@C had excellent stability for overall water splitting in alkaline solution. The excellent activity and high stability of the catalyst are due to the high intrinsic activity of Ni_3N as well as the formation of carbon coating layer, which not only improves the conductivity of the material and accelerates the transfer of electrons and protons, but also protects Ni_3N from corrosion in alkaline electrolyte. In a word, we provide a simple, economical and low-temperature sustaining method to prepare Ni_3N to be used in water splitting, and the preparation method can also be used to prepare other promising bifunctional electrocatalysts for energy conversion field.

Keywords: Nickel Nitride, Electrocatalysis, Bifunctional, Water Splitting, Hydrogen Energy

INTRODUCTION

The transformation and storage of renewable clean energy has become the best way to solve the fossil energy crisis [1]. At present, hydrogen is an ideal green energy carrier, which not only has good storability, but can be stored and transported on a large scale. It also has very high energy mass density, good combustion performance, and the burning final product is water, which means that it can be recycled with zero carbon emission, friendly to the environment and no pollution. On the other hand, hydrogen production from electrocatalysis of water can transform the electricity into hydrogen energy with excellent storage performance [2], which has the advantages of non-pollution, high safety and reliability; thus, it is considered as the most potential technology. The key half reactions of water splitting include hydrogen evolution reaction (HER) and oxygen evolution reaction (OER), among which, HER is difficult to form bonded protons in alkaline solution [3]; OER involves a multi proton-coupled electron transfer step, which has intrinsically sluggish kinetics [4]. Thus, advanced electrocatalysts (ECs) to accelerate the reaction kinetics and reduce overpotential (η) for OER and HER are badly in need of development, and the reasonable design of high-performance ECs is particularly important.

The materials that can realize the OER or HER with better energy efficiency are mainly focused on Pt (for HER), IrO_2 and RuO_2 for OER [5-8]. The scarcity and high cost of these precious metal ECs have greatly restricted their widespread application, hindering the successful application and large-scale hydrogen production. Therefore, it is imperative to find new non-noble metal ECs with low price and good catalytic performance that can realize the overall water splitting. In recent years, transition metal nitrides were introduced to show good electrocatalytic efficiency [9-14]. Transition metal nitrides are formed by the insertion of N atoms into the metal lattice, where the lattice expands, the interaction force between metal atoms weakens, and the structure changes, which makes metal nitrides have unique physical and chemical properties [15,16]. Among them, nickel based nitrides have gained wide attention owing to their environmental friendliness, high abundance and unique electronic structure, along with promising catalytic activity and stability in water splitting [9,11,12]. For example, Chen et al. [17] prepared a sponge-like Ni_3N/NC, which showed η of 310 mV at a current density of 10 mA cm^{-2} for OER. Ouyang et al. [18] grew hierarchical Ni_3N on nickel foam, and the prepared catalyst showed η of 325 mV at a current density of 10 mA cm^{-2} for the OER in alkaline solution. In addition, nickel nitrides, such as NiMoN were demonstrated to show excellent HER catalytic activity and good stability in acidic media [19,20]. Gong et al. [21] prepared NiMoN micro-pillar arrays on nickel foam, showing excellent HER performance in acidic medium, where η was 31 mV at 10 mA cm^{-2}. Gao et al. [22] synthesized Ni_3N-nanosheets, which showed η of 59 mV for HER in acidic media at 10 mA cm^{-2}, but its η for HER in

†To whom correspondence should be addressed.
E-mail: banghuapeng@163.com

alkaline solution was 305 mV at 10 mA cm^{-2}.

From the above articles, it can be seen that transition nickel nitrides have attracted much attention due to their high conductivity and good catalytic activity for HER and OER in solution. However, it is still a great challenge to develop ECs with HER/OER bifunctional activity, especially for HER and water splitting in alkaline solution. Secondly, nickel nitrides are commonly synthesized by thermal treatment at high temperature using corresponding metal oxides as precursors and ammonia, nitrogen gas or nitrogen-containing organics as nitrogen sources [23-25]. Most of these studies have been using complex synthesis methods to obtain nickel nitrides, which can only capture a small amount of nitrogen element because metastable nickel nitride usually exhibits limited thermal stability, and high temperature will reduce metal nitrides to metal elements [26,27]. Usually the conductive substrate is necessary to support nickel nitride and contribute to the electrons transportation, while it is difficult to synthesize nickel nitride with conductive layer by a low temperature one-step synthesis method.

In this work, Ni_3N@C nanocomposites were synthesized by one-step low-temperature pyrolysis method using $Ni(CH_3COO)_2{\cdot}4H_2O$ as Ni and C source, NH_3 as N source. Spherical Ni_3N nanoparticles were formed uniformly coated with a carbon protective layer with a thickness of 10 nm, which showed excellent HER and OER activity in alkaline solution and can be used as bifunctional catalyst for overall water splitting. Due to the excellent intrinsic activity of Ni_3N and carbon protective layer, the as-prepared Ni_3N@C hybrids exhibited excellent activity and stability toward HER and OER, showing low onset potential and η of 284 mV and 390 mV for HER and OER at the current density of 10 mA cm^{-2}, respectively. One-step pyrolysis is a simple, scalable, and versatile approach for preparation Ni_3N, which is expected to become a candidate material for high efficiency overall water splitting catalyst.

EXPERIMENTAL SECTION

1. Materials

Nickel acetate ($Ni(CH_3COO)_2{\cdot}4H_2O$) was purchased from Tianjin Chemical Reagent Research Institute. Polytetrafluoroethylene concentrated dispersion (PTFE, 60 wt% water suspension) was the product of Shanghai Crystal Pure Biological Technology Co., Ltd. Carbon fiber paper (CFP) was bought from Shanghai Hesen Electric Co., Ltd. All the chemicals in this study were used without further purification.

2. Synthesis of Ni_3N@C Hybrid Catalyst

500 mg of $Ni(CH_3COO)_2{\cdot}4H_2O$ was ground in the agate mortar and then heated to 350 °C for 2 h under a NH_3 atmosphere with a ramp rate of 5 °C min^{-1} in a tubular furnace. After cooling to room temperature, the resulting product Ni_3N@C was harvested.

3. Structural Characterization

The crystalline phases of the powder were determined by X-ray diffraction (XRD, Bruker D8 Advance) using Cu Kα (λ=0.154056 nm) radiation under 40 kV and 40 mA condition with scanning over the range of $20^\circ \le 2\theta \le 90^\circ$. The field emission scanning electronic microscope (SEM) images were performed on a Hitachi S-4800. The high-resolution transmission electron microscopy (HRTEM) was taken on a field JEM 2100 with the energy dispersive spectroscopy (EDS) and mapping equipment. Surface composition and valence state of element were investigated by X-ray photoelectron spectroscopy (XPS) with a monochromatized X-ray source (Al Kα hv=1,486.6 eV) (AMICUS ESCA3200). All binding energies were calibrated using carbon (C_{1s}=284.6 eV) as a reference.

4. Electrochemical Measurements

OER and HER measurements were carried out in a standard three electrodes system on a CHI 760D electrochemistry workstation (Chenhua Company, Shanghai) in an electrolyte solution of 1 M KOH using Ag/AgCl electrode as the reference electrode, graphite rod as the counter electrode, and CFP loaded with catalyst was used as the working electrode. In a typical procedure, 2 mg of catalyst was dispersed in 490 μL of water, 500 μL of ethanol and 10 μL of 10 wt% PTFE (from its 60 wt% water suspension). The mixed solution was sonicated at least for 30 min to form a homogeneous ink, and then 100 μL of dispersion (containing 0.2 mg of catalyst), divided into three times, was dropped onto 1 cm^2 CFP substrate, with loading about 0.2 mg cm^{-2}. The working electrode was cycled ~50 times by cyclic voltammetry (CV) with a scan rate of 50 mV s^{-1} until a stable CV curve was obtained, and polarization curves of the catalyst with linear sweep voltammetry (LSV) were measured at room temperature with a scan rate of 5 mV s^{-1}.

Overall water splitting was done by two-electrode system with Ni_3N@C as both cathode and anode in 1 M KOH. All the potentials E measured in this study were converted to reversible hydrogen electrode (RHE) scale according to the Nernst equation: $E_{vs\ RHE} = E_{vs\ Ag/AgCl} + 0.05916 \times pH + 0.197$ V. η was calculated as follows: $\eta = E_{vs\ RHE} - 1.23$ V.

The galvanostatic stability for HER, OER and overall water splitting was all sustained for 10 h at a constant current density. Electrochemical impedance spectroscopy (EIS) was carried out in a standard three electrode system on a CHI 760D with the scanning frequency 100 kHz-0.1 Hz, and the disturbance amplitude was 5 mV. The electrical double layer capacitor (C_{dl}) of the as-synthesized materials was measured in 1 M KOH from double-layer charging curves using CV at scan rates 10, 30, 50, 70, 90, 110, 130 and 150 mV s^{-1} in a small potential range of 1.12-1.22 V (vs RHE) without electrochemical reactions.

RESULTS AND DISCUSSION

The crystal structure of the obtained catalysts was characterized by XRD as shown in Fig. 1. All the peaks are identical well with the crystallographic phase of Ni_3N nanocrystal (JCPDS No. 10-0280), in which the well-defined diffraction peaks at 2θ values of 38.92°, 41.90°, 44.43°, 58.50°, 70.46°, 78.29°, 83.64°, 85.46° and 87.25° were attributed to (110), (002), (111), (112), (300), (113), (220), (302) and (221) crystal planes, respectively, indicating good crystallinity of the Ni_3N particles [28]. It is clear that there is an inconspicuous small peak at 2θ value of 30.46°, which may be the amorphous carbon generated in the thermal decomposition process. Due to the large grain size and strong crystal quality of Ni_3N, the carbon peak is small. In addition, no characteristic peaks of the impurity are observed in the pattern.

The morphology of the prepared composite was investigated by SEM. As depicted in Fig. 2(a), the product obtained after pyrolysis

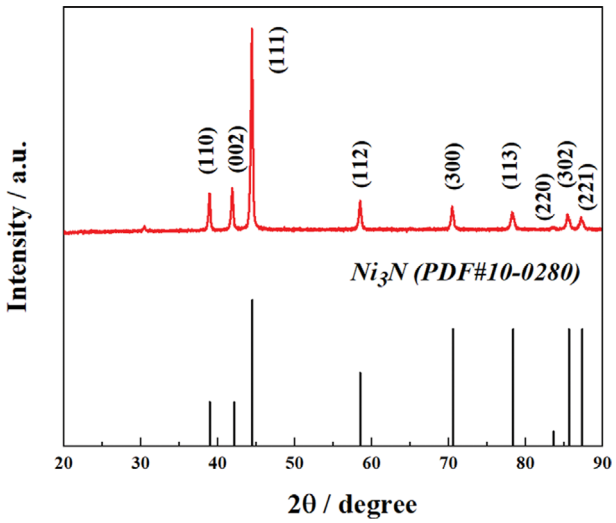

Fig. 1. XRD pattern of Ni_3N@C nanocomposite.

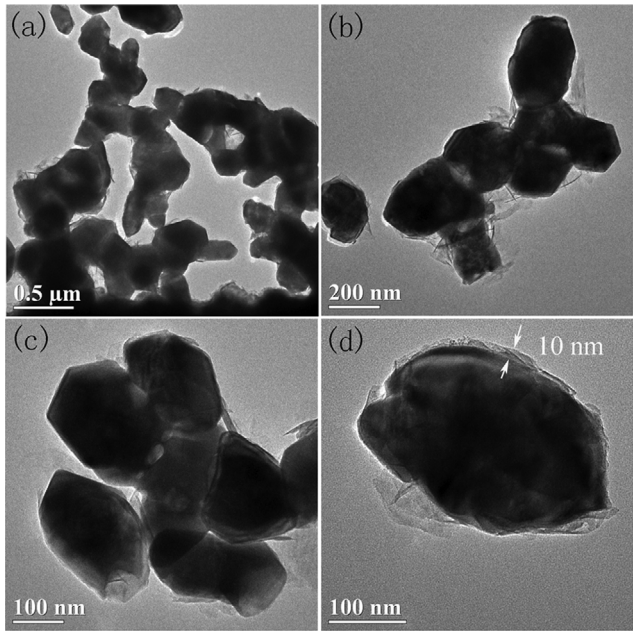

Fig. 3. TEM images of Ni_3N@C nanocomposite (a)-(b) at low magnification and (c)-(d) at high magnification.

at 350 °C for 2 h has good dispersion and no large agglomeration occurs, which indicates that the nanocomposites prepared through one-step pyrolysis method have good dispersion and uniform size. A high-magnification SEM image shown in Fig. 2(b) reveals the spherical nanoparticles are with diameter around 200 nm.

The morphology, crystalline state and dispersion of as-synthesized nanocomposites were further characterized by TEM (Fig. 3). As shown in Fig. 3(a) and 3(b), it is further confirmed the large-scale formation of the monodispersed spherical nanoparticles are with predominantly 200 nm in diameter, which is consistent with the SEM result. There are some thin sheets filled in the cracks of particles and wrapped around Ni_3N particles. Interestingly, TEM images shown in Fig. 3(c) and 3(d) reveal a thin layer of about 10 nm thickness is found around Ni_3N nanoparticles, and it is speculated that it might be a carbon coated layer. The coating structure can not only enhance the corrosion resistance of metal active sites, but also improve the electrical conductivity of N_3N, which will benefit the electrocatalytic reaction.

HRTEM image of Ni_3N@C nanoparticles given in Fig. 4 indicates the clear lattice spacing of 0.203 nm can be well assigned to the (111) plane of Ni_3N nanoparticles, which is in good agreement with the XRD pattern.

To further verify the successful synthesis of Ni_3N@C nanocomposite, especially the carbon coating layer, elemental analysis was performed by EDS. Fig. 5(a) indicates the presence of elements Ni, N, C, a handful of O for Ni_3N@C. The atomic ratio of Ni with N is 67.86 : 16.89, which is close to that of stoichiometric Ni_3N (3 : 1), and the carbon content in hybrid is 2.82% according to its weight percentage, proving the existence of C elements. The presence of O element may be due to a little oxidation of specimen. The elemental distribution for Ni_3N@C hybrids was further characterized by HAADF-STEM (high angle annular dark field-scanning transmission electron microscopy) and corresponding elemental mappings, as shown in Fig. 5(b)-(d). It is remarkable that different colors are used to distinguish the distributions of Ni (indicated by yellow color) and C (indicated by red color) elements. The brighter color indicates that the element is more concentrated in these regions. Both the Ni and C elements are found with homogeneous distribution in the composite, which further confirms the existence of C elements, and no detectable impurities exist. Unified with XRD

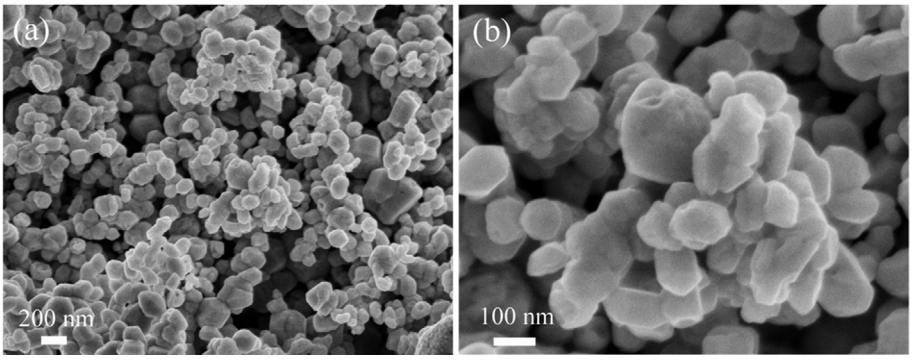

Fig. 2. SEM image of Ni_3N@C nanocomposite (a) at low magnification and (b) at high magnification.

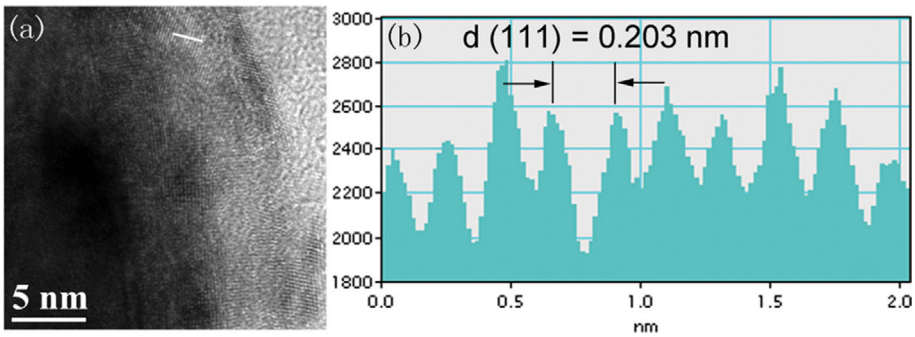

Fig. 4. (a) HRTEM image of Ni_3N@C; (b) Corresponding line profile of Ni_3N@C.

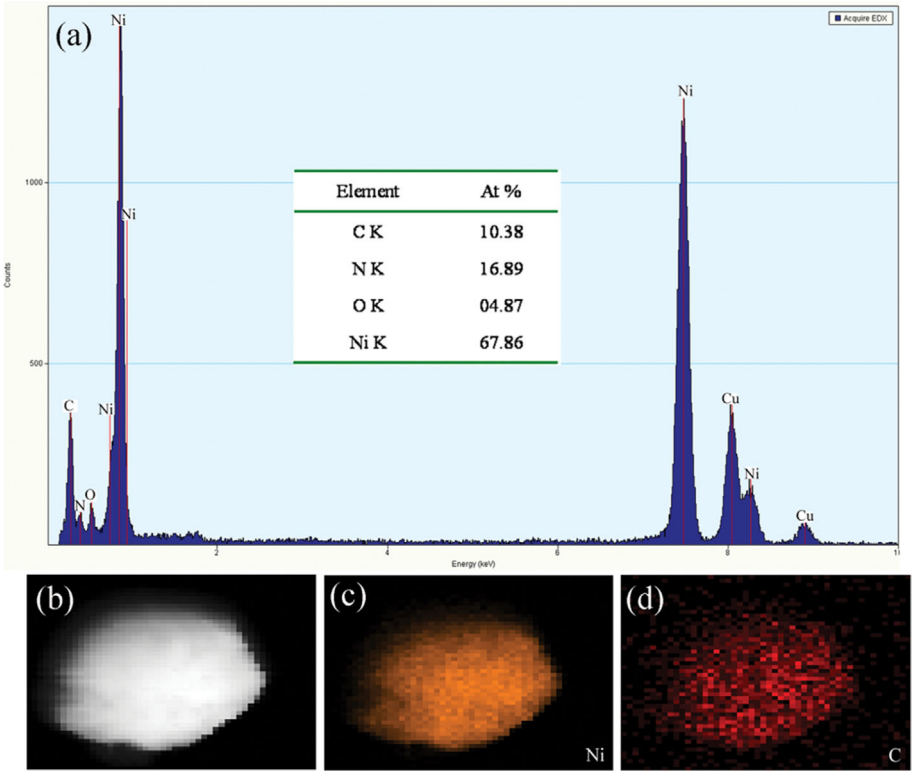

Fig. 5. (a) The EDS spectra of the Ni_3N@C hybrids; (b) HAADF-STEM image and corresponding elemental mapping images of (c) Ni and (d) C for the as-synthesized Ni_3N@C nanocomposite.

and TEM, it is verified that the carbon coated Ni_3N nanoparticles are successfully synthesized.

To further observe the surface elemental composition and the electronic configuration for Ni_3N@C nanocomposites, the XPS was performed. Fig. 6(a) shows the overall XPS spectrum of Ni_3N@C hybird, also indicating the presence of element Ni, N, C and O. As depicted in Fig. 6(b), the deailed Ni 2p XPS spectrum divided by spin-orbit coupling with binding energy at 854.5 eV (Ni $2p_{3/2}$) and 872.2 eV (Ni $2p_{1/2}$) is assigned to Ni^+ species. Peaks at 854.9 eV, 875.9 eV are considered as $2p_{3/2}$ and $2p_{1/2}$ for Ni^{2+}. There are still two satellite peaks located at 858.1 and 883.1 eV, respectively [29, 30]. All these measurement results indicate that Ni_3N@C surface is slightly oxidized and the introduction of N optimizes the charge distribution for nickel, which promotes the formation of nickel nitride with good conductivity and catalytic activity [31]. Note that the N 1s peak Fig. 6(c) can be deconvoluted into two components, of which binding energy at 397.7 eV is from N in Ni_3N, and the signal at 399.7 eV is derived from C-N-C, meaning that partial nitriding effect of carbon coating. In addition, the C 1s peak Fig. 6(d) also can be deconvoluted into two types, binding energies at 284.8 eV and 287.6 eV, indicating that the presence of C-C and C-N-C, respectively.

To evaluate the catalytic properties of Ni_3N@C hybrids for HER and OER, the sample was first homogeneously deposited on CFP with a catalyst loading of 0.2 mg cm^{-2}. LSV polarization curves using the prepared electrode were evaluated in 1 M KOH solutions using a standard three-electrode system at 5 mV s^{-1} to minimize the capacitive current. As shown in Fig. 7, the polarization curves showed

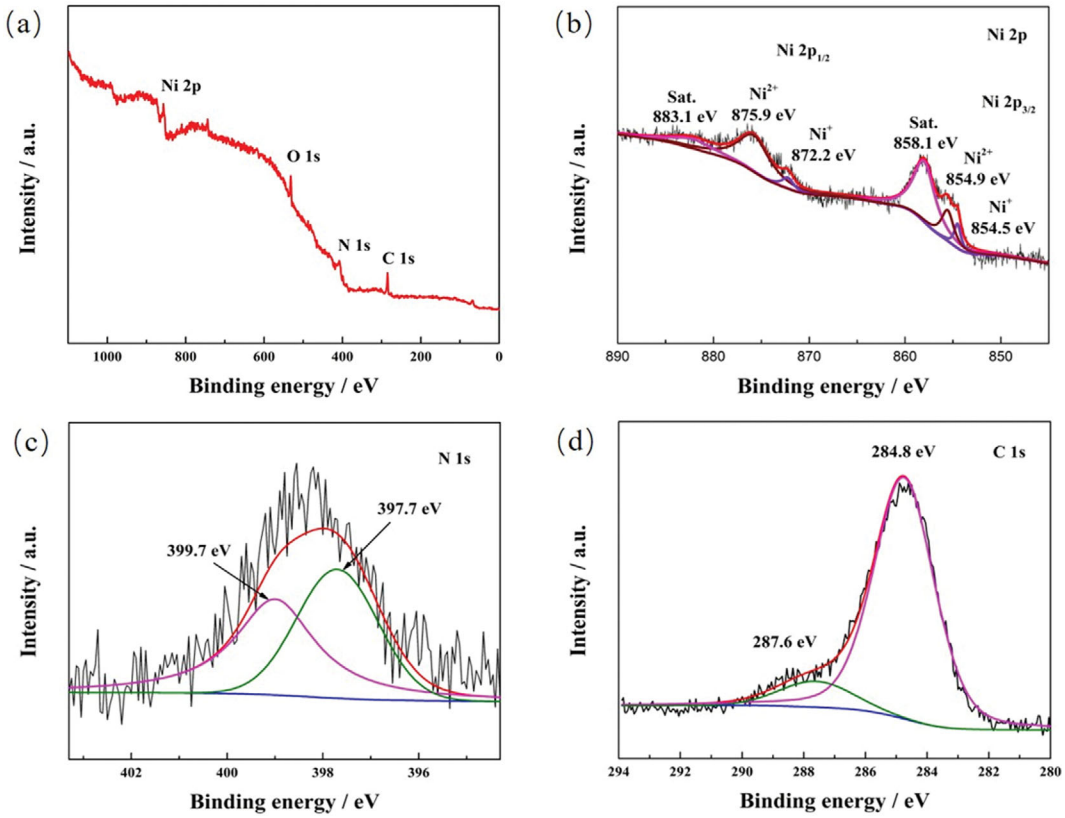

Fig. 6. (a) XPS survey spectra of Ni_3N@C nanocomposite; (b), (c) and (d) are deconvoluted Ni 2p, N 1s and C 1s XPS spectra.

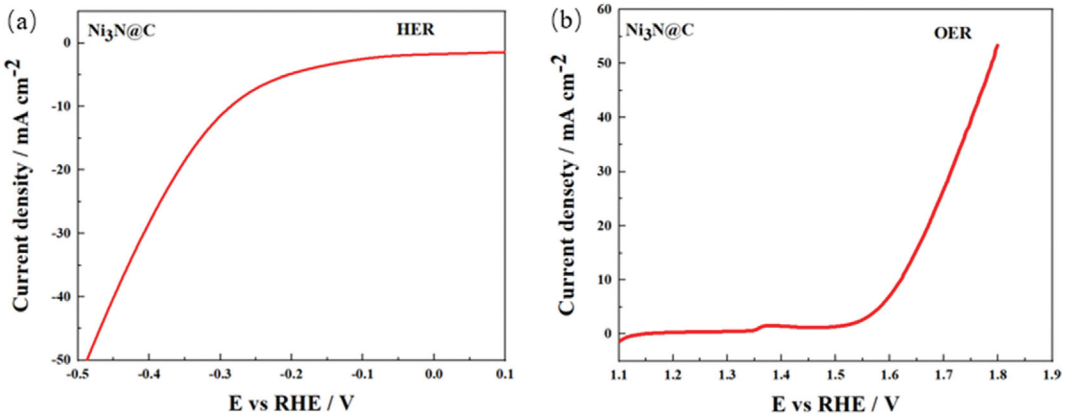

Fig. 7. LSV curve of Ni_3N@C in 1 M KOH (a) for HER and (b) for OER.

that they had excellent catalytic activity for HER and OER in alkaline solution. The initial potentials are −0.06 V (vs RHE) for HER and 1.53 V (vs RHE) for OER, with a small η of 284 mV and 390 mV at a current density of 10 mA cm^{-2}, respectively. The high catalytic performance for Ni_3N@C nanocomposite could be attributed to the following two reasons. First, the dominant factor of Ni_3N nanoparticles obtained by one-step pyrolysis is good choice for Ni based catalysts. Second, the coated carbon layer formed in-situ can conduct electrons as a channel, and plays an important role in enhancing the conductivity of the composites.

To further analyze the kinetic characteristics of the catalyst, we conducted an EIS test on Ni_3N@C and simulated the equivalent circuit in Fig. 8. Here, the intersection value on the horizontal axis at the high frequency is the uncompensated solution resistance R_s. The diameter of the semicircle in the Nyquist plot reflects the R_{ct} value, which represents the charge transfer resistance at the interface between the electrolyte solution and the electrode. As can be seen, CFP shows a large semi-circle; thus, the high frequency region is magnified to obtain the inset figure in Fig. 8. In the inset, R_s is almost the same for CFP and Ni_3N@C, but the diameter of Ni_3N@C is smaller, indicating that R_{ct} value of Ni_3N@C is much lower than that of CFP. The smaller R_{ct} illustrates the interfacial resistance be-

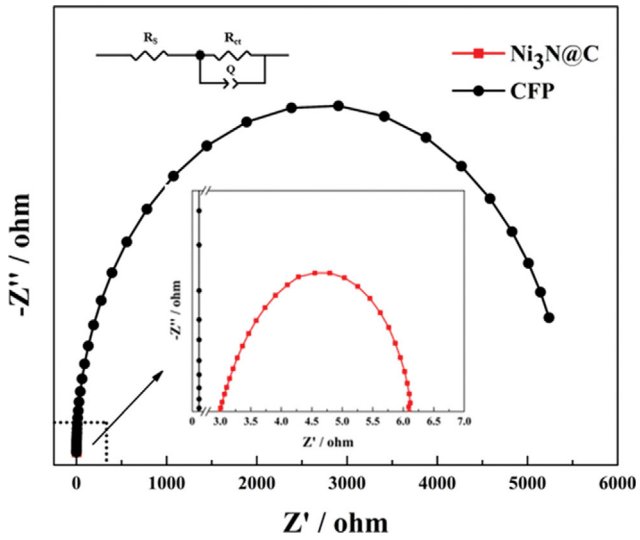

Fig. 8. Nyquist plots of Ni_3N@C and CFP (the inset in the upper left corner shows the corresponding equivalent electric circuit and the figure in the middle is the enlarged view at high frequency region).

tween the ECs and the solution is small, and Ni_3N@C has good conductivity, thus leading to fast reaction speed.

In addition, the electrochemically active surface area (ECSA), that is, the effective area involved in the electrochemical reaction, is also one of the important parameters for studying the kinetic process of Ni_3N@C. As shown in Fig. 9(a)-(b), CV curves of Ni_3N@C and CFP with different scanning rates were tested in the potential range of 1.12-1.22 V (vs RHE). As shown in Fig. 9(c), when the potential value was fixed at 1.17 V (vs RHE), the current density difference Δj for Ni_3N@C and CFP had a linear relationship with the scanning speed, and the slope is the double-layer capacitance value C_{dl}, which for Ni_3N@C is 167.4 μF cm^{-2} and for CFP is 57.45 μF cm^{-2} (Fig. 9(c)). Under the same test conditions, the C_{dl} value is directly proportional to the ECSA. It is obvious that compared with CFP, the ECSA of Ni_3N@C increases significantly, indicating more active sites are exposed.

In addition to good catalytic activity, it also showed excellent stability. Fig. 10(a) shows the chronopotentiometric response of OER for Ni_3N@C nanocomposites under static current density of 10 mA cm^{-2}. After a long period 10 h, the potential varies between 1.616 V and 1.631 V (vs RHE), and significant changes do not occur, indicating Ni_3N@C hybrids exhibit strong stability. The inset shows that the Ni_3N@C hybrid almost affords the same the LSV polarization curve as initial catalyst even after 10 h galvanostatic measurement. The protective coated carbon layer formed in-situ transported electrons as a channel, and played an important role in protecting Ni_3N nanoparticles and avoiding the corrosion of active sites in alkaline solution, thus improving the stability of the catalyst.

Fig. 10(b) shows the potential response of HER for Ni_3N@C nanocomposites under 20 mA cm^{-2}. It is obvious that Ni_3N@C

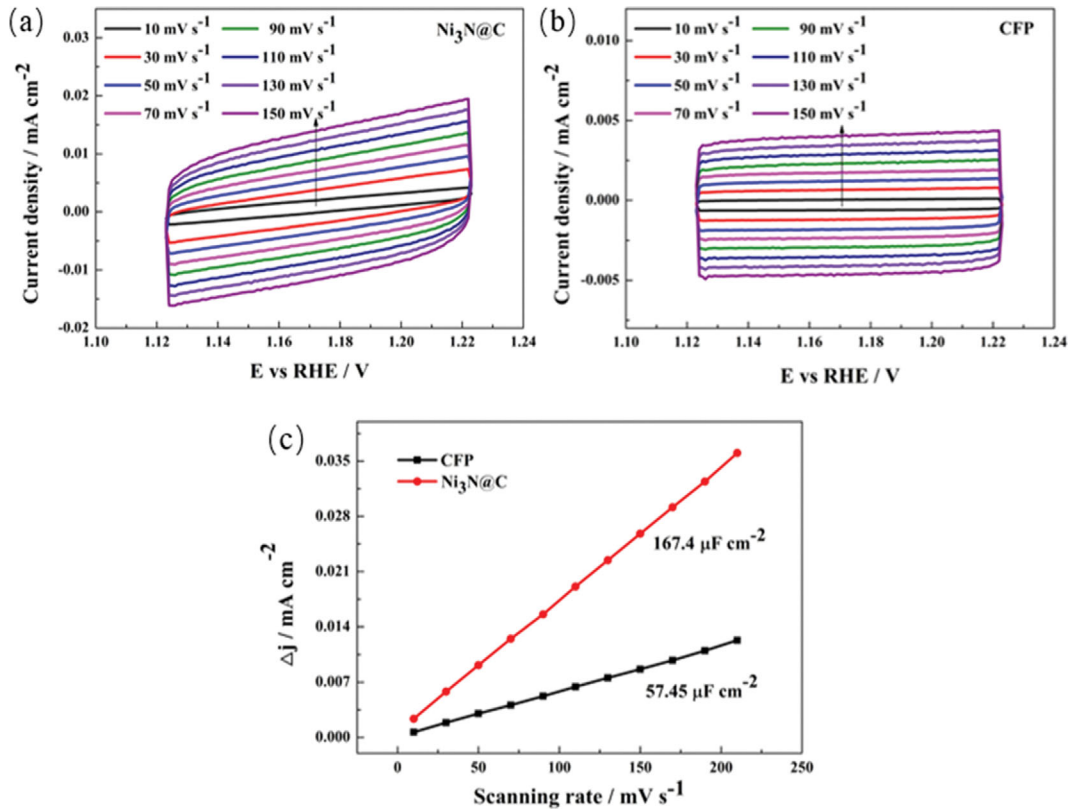

Fig. 9. CV curves of (a) Ni_3N@C and (b) CFP at different scanning rates; (c) Comparison of the linear relationship of current density with scanning rates for Ni_3N@C and CFP.

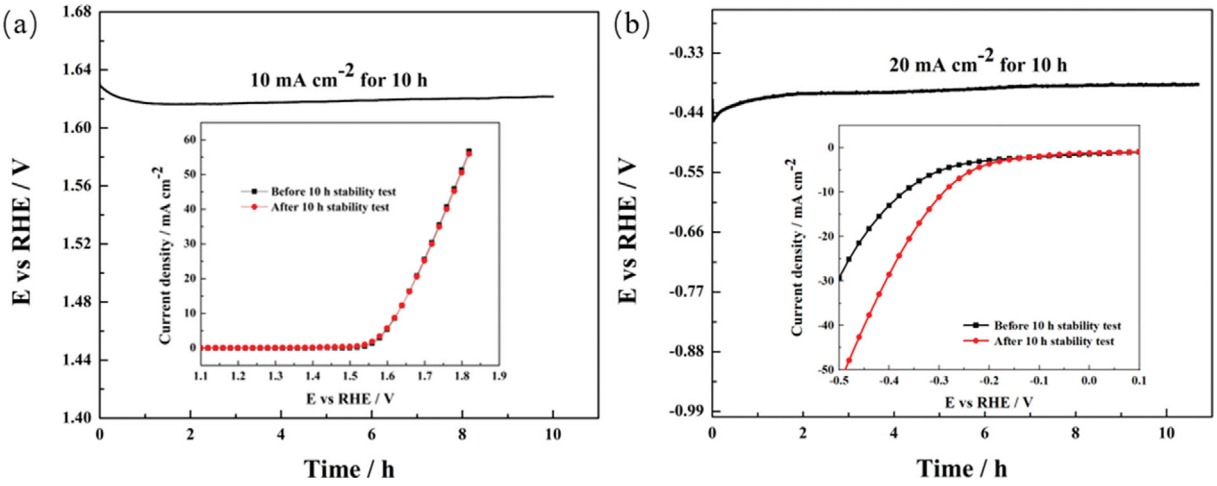

Fig. 10. (a) Chronopotentiometric curve of Ni_3N@C nanocomposite for OER at a constant current density of 10 mA cm^{-2} (the inset shows the polarization curves of OER for hybrids before and after 10 h stability test); (b) Chronopotentiometric curve of Ni_3N@C nanocomposite for HER at a constant current density of 20 mA cm^{-2} (the inset shows the polarization curves of HER for hybrids before and after 10 h stability test).

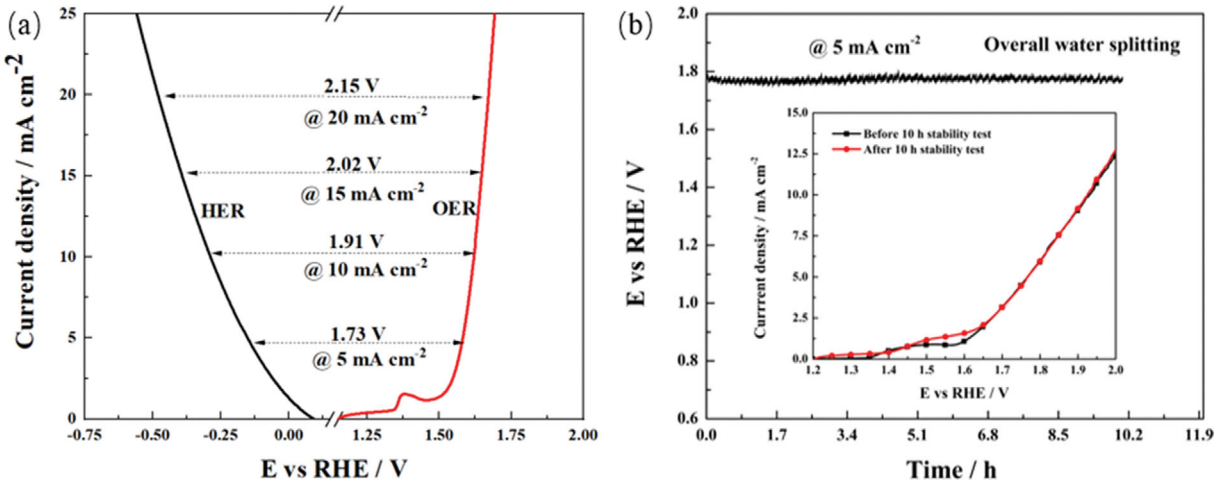

Fig. 11. Overall water splitting performance of Ni_3N@C in 1.0 M KOH using two-electrode Ni_3N@C//Ni_3N@C system (a) HER and OER LSV polarization curves of Ni_3N@C; (b) Chronopotentiometric curve of Ni_3N@C nanocomposite for overall water splitting at a constant current density of 5 mA cm^{-2} (the inset shows the polarization curves before and after 10 h stability test).

nanocomposite also has a good HER stability, which is rare in alkaline solution. The inset is the LSV polarization curve of Ni_3N@C before and after the stability test for 10 h. Surprisingly, after 10 h stability test, the HER initial potential of Ni_3N@C decreased by 36 mV, and η of Ni_3N@C decreased by 80 mV at the current density of 10 mA cm^{-2}, which may be due to the fact that in the long-term HER process, the hydrogen produced in large amounts breaks away from the catalyst surface and leaves a vacancy to form a porous structure, making the active sites increased and more conductive to improve the activity of HER. The intrinsic reason for the enhanced HER performance will be further studied in the next step.

The excellent bifunctional electrocatalytic activity for HER and OER prompts us to design two-electrode system for water splitting. Ni_3N@C deposited on CFP were used as both cathode and anode (Ni_3N@C//Ni_3N@C) in 1.0 M KOH. The LSV polarization curves were evaluated at a scanning speed of 5 mV s^{-1}. Fig. 11(a) shows the polarization curves of HER and OER placed on the same coordinate axis, and the potential corresponding to current density in the two-electrode system can be judged through the potential difference (voltages) on the curves. It can be clearly seen from the figure that the voltage between HER and OER is 1.73 V, 1.91 V, 2.02 V and 2.15 V, respectively, when the current density reaches 5, 10, 15 and 20 mA cm^{-2}, which indicates that Ni_3N@C is a highly efficient and energy-saving catalyst for overall water splitting. At the same time, the stability of Ni_3N@C for overall water splitting was measured at a constant current of 5 mA cm^{-2}, and it can be seen that the voltage has no downward trend during the 10 h electrolysis process (Fig. 11(b)). The overlapped LSV curves of before and after the overall water splitting 10 h stability test also have no obvious changes (inset in Fig. 11(b)), which further reveals the

high activity and durability of Ni_3N@C for overall water splitting.

CONCLUSION

Using $Ni(CH_3COO)_2{\cdot}4H_2O$ as a precursor, a one-step pyrolysis method was successfully developed to synthesize carbon-coated Ni_3N nanocomposite. The uniformly distributed Ni_3N nanoparticles with an average size of ~200 nm are well dispersed and have carbon layer formed in-situ about 10 nm. Thanks to its intrinsic high activity and good dispersion, Ni_3N@C shows a low HER initial potential, which is only - 60 mV and a low OER starting potential of 1.53 V vs RHE. At the same time, the catalyst shows excellent stability for HER and OER in alkaline solution for about 10 h. In an alkaline electrolytic cell, using Ni_3N@C as cathode and anode, an initial voltage of only 1.60 V is required to activate the cell and a low voltage of 1.91 V is needed for water splitting at 10 mA cm^{-2}. Meanwhile, the catalyst shows long-term stability. The high performance of the as-prepared Ni_3N@C nanocomposite is associated with the highly active nature of Ni_3N, along with electrical conductivity of carbon formed in-situ, promoting electron transfer of the electrode surface and protecting catalyst from corrosion, which are favorable to improve activity and stability for the HER, OER and overall water splitting. This study may open up a new avenue for the design and syntheses of non-noble overall water splitting ECs toward energy conversion and storage applications.

ACKNOWLEDGEMENTS

This work was supported by the National Natural Science Foundation of China (21663023).

AUTHOR CONTRIBUTIONS

Authors Banghua Peng, Jianning Wu and Feng Yu proposed an experimental approach; authors Weilin Weng and Jianhong Chen carried out synthesis of samples, performed their electrochemical study, XPS spectroscopy, TEM analysis and XRD techniques; authors Zhiyong Liu and Qingcui Liu took part in preparation of the manuscript; all authors participated in discussion of results.

CONFLICTS OF INTEREST

There are no conflicts to declare.

REFERENCES

1. Y. Li, Y. B. Li, P. F. Ji and J. Yang, *Renew. Sust. Energ. Rev.*, **49**, 805 (2015).
2. A. Ursua, L. M. Gandia and P. Sanchis, *IEEE*, **100**, 410 (2012).
3. S. Anantharaj, S. Noda, V. R. Jothi, S. Yi, M. Driess and P. W. Menezes, *Angew. Chem. Int. Ed.*, **60**, 18981 (2021).
4. N. T. Suen, S. F. Hung, Q. Quan, N. Zhang, Y. J. Xu and H. M. Chen, *Chem. Soc. Rev.*, **46**, 337 (2017).
5. C. Li and J. B. Baek, *ACS Omega*, **5**, 31 (2020).
6. W. Lu, J. Chen, J. Feng and J. Yu, *Rare. Metal Mat. Eng.*, **41**, 184 (2012).
7. R. Sun, W. Guo, X. Han and X. Hong, *Chem. Res. Chin. U.*, **36**, 597 (2020).
8. L. Tian, Z. Li, M. Song and J. Li, *Nanoscale*, **13**, 12088 (2021).
9. S. H. Gage, B. G. Trewyn, C. V. Ciobanu, S. Pylypenko and R. M. Richards, *Catal. Sci. Technol.*, **6**, 4059 (2016).
10. N. Han, P. Liu, J. Jiang, L. Ai, Z. Shao and S. Liu, *J. Mater. Chem. A*, **6**, 19912 (2018).
11. M. Shalom, D. Ressnig, X. Yang, G. Clavel, T. P. Fellinger and M. Antonietti, *J. Mater. Chem. A*, **3**, 8171 (2015).
12. A. K. Tareen, G. S. Priyanga, K. Khan, E. Pervaiz, T. Thomas and M. Yang, *ChemSusChem*, **12**, 3941 (2019).
13. Y. Wang, C. Xie, D. Liu, X. Huang, J. Huo and S. Wang, *ACS Appl. Mater. Inter.*, **8**, 18652 (2016).
14. Y. Zhang, B. Ouyang, J. Xu, G. Jia, S. Chen, R. S. Rawat and H. J. Fan, *Angew. Chem. Int. Ed.*, **55**, 8670 (2016).
15. R. Qin, P. Wang, C. Lin, F. Cao, J. Zhang, L. Chen and S. Mu, *Acta Phys-Chim. Sin.*, **37**, 2009099 (2021).
16. J. Zheng, W. Zhang, J. Zhang, M. Lv, S. Li, H. Song, Z. Cui, L. Du and S. Liao, *J. Mater. Chem. A*, **8**, 20803 (2020).
17. M. X. Chen, J. Qi, D. Y. Guo, H. T. Lei, W. Zhang and R. Cao, *Chem. Commun.*, **53**, 9566 (2017).
18. B. Ouyang, Y. Q. Zhang, Z. Zhang, H. J. Fan and R. S. Rawat, *Small*, **13**, 1604265 (2017).
19. B. Chang, J. Yang, Y. Shao, L. Zhang, W. Fan, B. Huang, Y. Wu and X. Hao, *ChemSusChem*, **11**, 3198 (2018).
20. W. F. Chen, K. Sasaki, C. Ma, A. I. Frenkel, N. Marinkovic, J. T. Muckerman, Y. Zhu and R. R. Adzic, *Angew. Chem. Int. Ed.*, **51**, 6131 (2012).
21. Y. Gong, L. Wang, H. Xiong, M. Shao, L. Xu, A. Xie, S. Zhuang, Y. Tang, X. Yang, Y. Chen and P. Wan, *J. Mater. Chem. A*, **7**, 13671 (2019).
22. D. Gao, J. Zhang, T. Wang, W. Xiao, K. Tao, D. Xue and J. Ding, *J. Mater. Chem. A*, **4**, 17363 (2016).
23. M.-S. Balogun, Y. Zeng, W. Qiu, Y. Luo, A. Onasanya, T. K. Olaniyi and Y. Tong, *J. Mater. Chem. A*, **4**, 9844 (2016).
24. S. H. Gage, D. A. Ruddy, S. Pylypenko and R. M. Richards, *Catal. Today*, **306**, 9 (2018).
25. M. Shalom, V. Molinari, D. Esposito, G. Clavel, D. Ressnig, C. Giordano and M. Antonietti, *Adv. Mater.*, **26**, 1272 (2014).
26. B. Alfons and M. Marek, *J. Chem. Soc., Faraday Trans. 1*, **80**, 2331 (1984).
27. Z. Wang, W. Yu, J. Chen, M. Zhang, W. Li and K. Tao, *J. Alloys Compd.*, **466**, 352 (2008).
28. H. Wang, J. Xiong, X. Cheng, M. Fritz, A. Ispas, A. Bund, G. Chen, D. Wang and P. Schaaf, *ACS Appl. Nano Mater.*, **3**, 10986 (2020).
29. W. Hua, H. Sun, H. Liu, Y. Li and J.-G. Wang, *Appl. Surf. Sci.*, **540**, 148407 (2021).
30. X. Liu, Y. Guo, P. Wang, Q. Wu, Q. Zhang, E. A. Rozhkova, Z. Wang, Y. Liu, Z. Zheng, Y. Dai and B. Huang, *ACS Appl. Energy Mater.*, **3**, 2440 (2020).
31. H. Jin, X. Wang, C. Tang, A. Vasileff, L. Li, A. Slattery and S. Z. Qiao, *Adv. Mater.*, **33**, 2007508 (2021).